A Supervised Learning Based Approach to Detect Crohn's Disease in Abdominal MR Volumes

Dwarikanath Mahapatra[1], Peter Schueffler[1], Jeroen A.W. Tielbeek[2], Joachim M. Buhmann[1], and Franciscus M. Vos[2,3]

[1] Department of Computer Science, ETH Zurich, Switzerland
dwarikanath.mahapatra@inf.ethz.ch
[2] Department of Radiology, Academic Medical Center, The Netherlands
[3] Quantitative Imaging Group, Delft University of Technology, The Netherlands

Abstract. Accurate diagnosis of Crohn's disease (CD) has emerged as an important medical challenge. Because current Magnetic resonance imaging (MRI) analysis approaches rely on extensive manual segmentation for an accurate analysis, we propose a method for the automatic identification and localization of regions in abdominal MR volumes that have been affected by CD. Our proposed approach will serve to augment results from colonoscopy, the current reference standard for CD diagnosis. Intensity statistics, texture anisotropy and shape asymmetry of the 3D regions are used as features to distinguish between diseased and normal regions. Particular emphasis is laid on a novel entropy based asymmetry calculation method. Experiments on real patient data show that our features achieve a high level of accuracy and perform better than two competing methods.

Keywords: Crohn's disease, supervised learning, magnetic resonance imaging.

1 Introduction

Inflammatory bowel diseases (IBDs) constitute one of the largest healthcare problems in the Western world afflicting over 1 million European citizens. Out of these, nearly 700,000 suffer from Crohn's disease (CD). Crohn's disease is a autoimmune IBD that may affect any part of the gastrointestinal tract causing abdominal pain, diarrhea, vomiting or weight loss. Assessment of CD severity is essential to determine the therapeutic strategy. Currently, the reference standard for diagnosis relies on results of colonoscopy and biopsy samples [13]. However, the procedure is invasive, requires extensive bowel preparation, and gives information only on superficial abnormalities. Therefore it is beneficial to have a non-invasive approach to detect CD.

Scope of Our Work: This paper proposes a method to *detect* and *localize* CD afflicted regions from input abdominal magnetic resonance (MR) volumes without an explicit segmentation of the bowel wall. Our method will serve as a tool

H. Yoshida, D. Hawkes, M.W. Vannier (Eds.): Abdominal Imaging 2012, LNCS 7601, pp. 97–106, 2012.

to assist clinicians, reduce reliance on colonoscopy and help in rapid diagnosis of CD. We extract features from 3D volumes of interest (VOI) and use them to detect diseased regions. Intensity statistics, texture anisotropy and curvature asymmetry were used as features to discriminate between diseased, normal and background (normal non-intestine) regions. Also, higher order intensity statistics like kurtosis and skewness that cannot be processed by the human visual system (HVS) [9] are used for disease classification. Anisotropy of features is a measure of a region's asymmetry and has been used for identifying tumorous regions [11]. We propose a novel entropy based method to calculate the texture anisotropy and curvature asymmetry of a VOI. Experimental results show a high degree of accuracy in detecting CD. This paper makes the following contributions: 1) an entropy based approach to calculate anisotropy and asymmetry of a region is proposed; 2) it is combined with higher order image statistics to identify CD affected areas in abdominal MRI. We describe our method in Section 2, present results in Section 3 and conclude with Section 4.

Related Work on Disease Classification: Several drawbacks of colonoscopy like invasiveness, procedure related discomfort and risk of bowel perforation has led to the exploration of imaging techniques like sonography, computed tomography (CT) and MRI to assess extension and severity of IBDs [17]. MRI has the potential to overcome limitations of sonography (gas interposition) and CT (exposure to ionising radiations) because of high tissue contrast, lack of ionising radiations and lower incidence of adverse events related to intravenous contrast. Rimola et al. in [17] determined that rate of contrast enhancement and bowel wall thickness relate to the severity of endoscopically active CD. However, its reliance on explicit segmentation of the bowel wall and extensive manual scoring limits its effectiveness.

There does not exist abundant research on image analysis of abdominal MRI to identify Crohn's disease, although [4] use dynamic contrast enhanced (DCE) MRI for identifying colorectal cancer and [18] deal with ulcerative colitis. Previous research has addressed the tasks of identifying abnormal regions in different applications like glaucoma diagnosis [7], whole body MR scans [15], cardiac coronary stenoses [10] and Alzheimer's disease [21] to name a few.

2 Methods

We employ a two stage classification approach where a test sample is first classified as either background or intestine. If the initial classification is intestine, then the sample is further classified as either diseased or normal. Manual annotations by experts indicating diseased, normal and background regions in 3D MR volumes were available. For every such labeled voxel we extract features (intensity statistics, texture anisotropy and shape asymmetry) from its $35 \times 35 \times 5$ neighborhood for training the classifiers.

Intensity and Texture Features: Since a simple visual examination of T1 MRI does not provide sufficient information to identify diseased areas, radiologists rely

on the results from different tests (like colonoscopy and biopsy), and imaging protocols like MR-T1, MR-T2 and DCE-MRI. It is common in MR images to have regions that do not form distinct spatial patterns but differ in their third order statistics, e.g. boundaries of some malignant tumours are diffuse and invisible to the naked eye [16]. We propose to investigate features that are not discernible by the human eye but may provide discriminating features for our task. In addition to mean and variance we calculate third and fourth order intensity statistics (like skewness and kurtosis) in a voxel's neighborhood.

In [11] texture anisotropy was used as a feature to identify tumorous regions in brain images. Normal tissues exhibit a regular pattern in their appearance while diseased regions show areas of asymmetry where the tissues have been affected by the progression of disease. We aim to exploit this characteristic to discriminate between diseased and normal regions in a VOI. Texture maps of the VOI were obtained using orthonormal Gabor filters in the $x-y$ and $y-z$ directions as described in [20] because 3D texture filters are computationally very expensive. Gabor filters conform to the receptive field properties of cortical cells, capture rich visual properties like spatial frequency characteristics and orientation, and are robust to noise by incorporating Gaussian smoothing. Texture maps are obtained along six directions $(0°, 30°, 60°, 90°, 120°, 150°)$ for each slice.

While anisotropy in [11] was calculated using local gradient differences and gray level dependence histograms, we use entropy to measure anisotropy. Texture maps of slices in the $x-y$ plane are divided into 9 equal parts corresponding to 9 sectors of a circle, and entropy determined for each sector. A higher entropy value indicates wider distribution of texture values (hence high anisotropy), while low entropy indicates lower anisotropy. The texture anisotropy for sector r is

$$Tex^r_{Anisotropy} = -\sum_{tex} p^r_{tex} \log p^r_{tex}. \tag{1}$$

p^r_{tex} denotes the probability of distribution of texture values in sector r. We use a different approach to calculate anisotropy of images in the $y-z$ plane. As there are 5 slices in the z dimension, there are not enough samples (only $35 \times 5 = 175$) to calculate a reliable measure of entropy. Instead we calculate the entropy for the whole slice and use it in the feature vector. Thus the number of texture features are 80 (9 entropy values from each of 5 slices in the $x-y$ plane, and 1 entropy value from each of 35 slices in the $y-z$ plane). Hence forth we shall denote the 80 dimensional texture feature vector as Tex. Fig. 1(e) shows the plot texture entropy values for two slices of diseased and normal patches.

Shape Asymmetry: We extend the concept of asymmetry (or anisotropy) to shape features. When healthy tissues are affected by progression of disease, it also affects spatial arrangement of voxels and hence their shape. Our aim is to exploit this irregularity for distinguishing between diseased and normal tissues. Shape features in the VOI are characterized by the 3D curvature of voxels. A detailed explanation of 3D curvature calculation is given in (http://www.cs.ucl.ac.uk/staff/S.Arridge/teaching/ndsp/curvature3D.pdf).

Shape asymmetry is calculated in a manner similar to texture anisotropy. The entropy of curvature values is determined from 9 sectors of each slice. If the curvature values have a wide distribution it indicates greater asymmetry in shape, leading to a higher entropy value. On the other hand low entropy values indicates less shape asymmetry. The shape asymmetry measure for a sector r is given by

$$Shape^{r}_{Asymmetry} = -\sum_{\theta} p^{r}_{\theta} \log p^{r}_{\theta}. \quad (2)$$

p^{r}_{θ} denotes the probability of distribution of curvature values in sector r, θ indicates the curvature values. Similar to texture anisotropy, the shape asymmetry measure is also a 80 dimensional feature vector. Henceforth the shape asymmetry vector is denoted as $Shape$. The above set of features give a 164 dimensional feature vector for a single 3D VOI.

Figs. 1(a) and (b) show a 2D patch around a diseased pixel, and the corresponding map of curvature values. Figs. 1(c) and (d) show a patch around a normal pixel and the corresponding curvature map. Figs. 1(e) and (f), respectively, show the plot of entropy values of texture and shape for 9 sectors of two slices from the VOI. The colormap of Figs. 1(b) and (d) are in the same range of $[0, 5]$, with red regions denoting regions of high curvature. The curvature profile for the normal patch is quite regular as compared to the diseased patch. This is indicative of the fact that the curvature in diseased regions becomes distorted due to ulcerations or other abnormalities. Thus they lose the regularity observed in healthy tissues. This is corroborated by the plot in Fig. 1(f) where the diseased patches show higher entropy indicating greater randomness.

3 Experimental Results

3D T1-weighted spoiled gradient echo sequence (SPGE) images were acquired from 26 patients in supine position using a 3-T MR imaging unit (Intera, Philips Healthcare). The spatial resolution of the images was 1.02 mm $\times$ 1.02 mm$\times$ 2 mm, and the acquired volume dimension was $400 \times 400 \times 100$ voxels. The number of annotated voxels were 6827 from diseased regions, 5156 from normal and 3725 from background regions. An expert radiologist annotated each diseased region by outlining the region on each corresponding slice.

Features and Classifiers: We compare our method with two others, namely the Dual-Complex Tree Wavelet Transform (DTCWT) based method of [3] ($DCTWT$) and a shape asymmetry based method derived from the reflectional asymmetry measure of [12] (Asy). These two methods are recent developments in the field of disease and asymmetry detection. Although our method uses more features than these methods, it also highlights the challenges of localizing areas affected with Crohn's diseases Each of the three methods was evaluated using three different classifiers, Random forests (RF), Support Vector Machines (SVM), and a Bayesian Classifier (BC). Random forests [5] have been successful in a variety of domains and compare favorably with other state-of-the-art

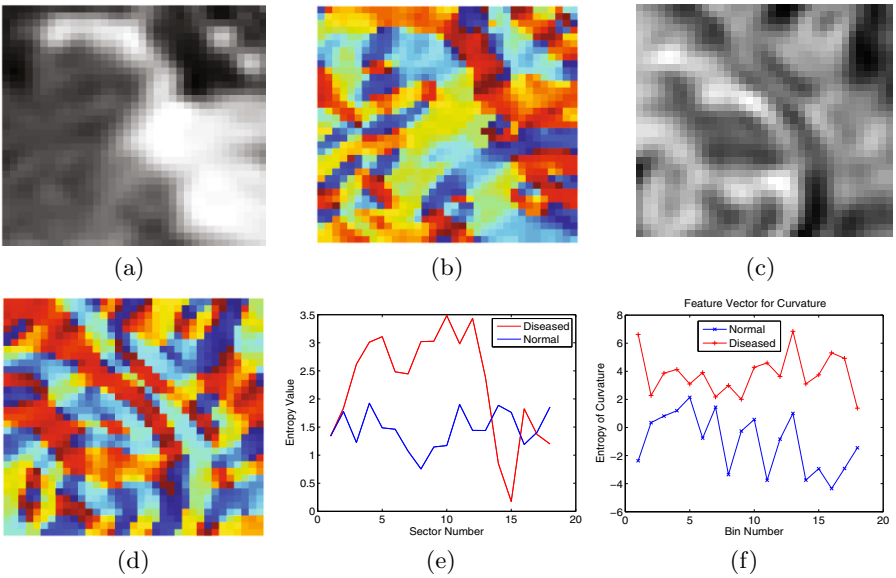

Fig. 1. (a)-(b) 2D patch around diseased voxel and corresponding curvature map; (c)-(d) normal patch and corresponding curvature map; plot of entropy values for (e) texture and (f) curvature of slices from VOI

algorithms [8]. A random forest is an ensemble of decision trees where each tree is trained with a different subset of the training data to improve the classifier's generalization ability. Training finds the set of tests that best separate the training data into different classes. Random forests and their variants have been used to detect abnormalities in mammograms [3], identify coronary artery stenoses [10] and semantic segmentation in CT images [14]. We use 50 trees for the RF classifier.

Support Vector Machines (SVMs) construct a hyperplane or set of hyperplanes in a high-dimensional space, which can be used for classification, regression, or other tasks. Intuitively, a good separation is achieved by the hyperplane that has the largest distance to the nearest training data of any class (so-called functional margin). In general larger the margin the lower the generalization error of the classifier. SVMs have also seen wide application in classification tasks like brain tumor segmentation [2,19], chest pathologies [1] and Glaucoma classification [7] among others. For SVMs we use the LIBSVM package [6] and define a radial basis function (RBF) as the kernel.

The default naive Bayesian classifier in MATLAB was the third classifier. A Bayesian classifier was chosen to highlight the linearly non-separable nature of the data, and the advantages of having a RBF kernel in SVMs. We have two classification stages for all classifiers. For all classifiers we employ 10−fold cross validation (leave-one-out with 10 subsets of the original data) approach.

Table 1. Quantitative measures for the *Stage* 1 classification using different features and three classifiers. Values indicate mean and standard deviation. Sensitivity is the number of correctly detected intestine samples. Specificity is the number of correctly detected background samples. Accuracy is the total of number of correct detections (both background and intestine samples).

	Asy			DTCWT			Our Features		
	SVM	BC	RF	SVM	BC	RF	SVM	BC	RF
Accuracy (%)	80.4 ±2.6	72.0 ±2.3	79.9 ±2.2	82.2 ±2.4	71.3 ±2.9	80.1 ±2.5	88.1 ±2.0	76.3 ±6.4	86.8 ±1.8
Specificity (%)	67.9 ±1.8	41.5 ±1.8	68.0 ±1.7	68.1 ±1.6	42.7 ±1.7	67.6 ±1.8	71.1 ±1.8	54.1 ±4.1	70.6 ±2.2
Sensitivity (%)	86.2 ±1.9	71.5 ±1.4	84.6 ±1.8	93.9 ±2.7	78.3 ±2.1	85.7 ±1.9	97.9 ±1.3	79.1 ±4.5	96.1 ±1.7

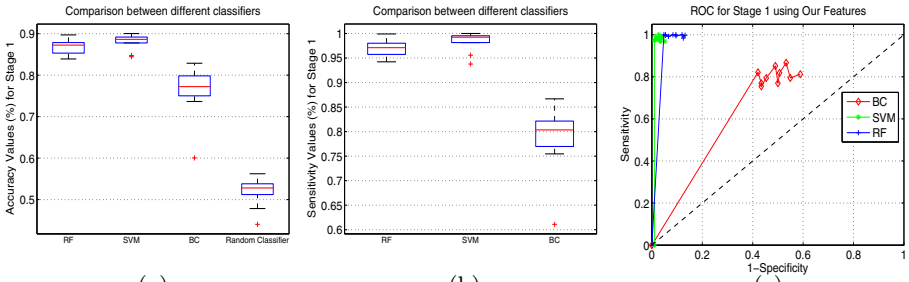

(a) (b) (c)

Fig. 2. Box plots for *Stage* 1 classification: (a) Accuracy; (b) Sensitivity. (c) ROC curves for three classifiers using our features.

Classification Results for Stage 1. Table 1 shows different quantitative measures of the first classification stage. Here each sample is classified as either intestine or background. The highest classification accuracy is obtained using our features, the results of which are shown in the box plots of Fig. 2. In this stage we desire a high sensitivity or true positive rate (TPR) even at the expense of low overall accuracy. True positive refers to a intestine sample correctly classified as intestine. We do not want a intestine sample to be incorrectly labeled as background thus increasing the false negative rate (FNR). In such a situation, the diseased samples (which are part of intestine in the first stage) get classified as background and hence escape the scrutiny of the next stage. This is particularly undesirable in a clinical decision making system.

A comparison of receiver operating characteristics (ROC) curves of all three classifiers using our features for stage 1 is shown in Fig. 2 (c). RF and SVM give high sensitivity (more than 90%), but their specificity values are comparatively lower indicating a large number of false positives, i.e., many background samples are classified as intestine. The overall accuracy (i.e., correct classification percentage of both intestine and background samples) is lower than 86% in all cases. This again indicates a high number of false positives. This is not a

Table 2. Quantitative measures for individual and different combination of features using RF classifier

	Int	Tex	$Shape$	$Tex + Int$	$Shape + Int$	$Shape + Tex$
Accuracy (%)	77.1±2.3	81.6±2.1	79.1±2.7	79.2±1.3	79.5±2.4	82.3±1.3
Sensitivity(%)	79.3±3.2	86.9±2.1	82.3±1.9	83.1±3.1	83.8±2.3	86.6±2.8

disadvantage since these incorrectly labeled background samples are invariably identified as normal in *Stage* 2 (as is evident from the results in Table 3 and Fig. 3). BC (which is good in classifying data with a linear decision boundary) has an overall accuracy less than 75%, which indicates the non-linearly separable nature of datasets. All classifiers perform better than a random classifier.

Importance of Different Features. Table 2 shows results of *Stage* 1 classification using individual features and their combinations. The combination of texture and shape features performs closest to the values in Table 1. However, this does not diminish the contribution of intensity. A Student t-test on the values for $Tex + Shape$ (Table 2)and $Our\ Features$ (Table 1) gives $p < 0.032$ indicating statistically different results ($p < 0.05$ indicates that the two sets of results are statistically different, and hence significant). t-tests between Tex and $Tex - Int$, and $Shape$ versus $Shape - Int$ give $p < 0.04$, showing that inclusion of intensity statistics contributes to significant improvement.

$DTCWT$ calculates a mean texture value across different orientations and scales while Tex calculates mean, variance, skewness and kurtosis across orientation and scales. Thus it is expected that Tex would be a more accurate measure than $DTCWT$, as reflected in Tables 2 and 1. Asy and $Shape$ provide similar information as indicated by results of $t-$tests ($p = 0.13$).

Classification Results for Stage 2. Intestine samples from *Stage* 1 are considered in *Stage* 2 for further classification into diseased or normal. Table 3 shows different quantitative measures for *Stage* 2 based on the *original* number of *diseased and normal* samples (not background samples) at the beginning of *Stage* 1. The values in Tables 1 and 3 are not directly related as Table 3 does not consider the background samples. In *Stage* 2 true positive refers to the number of correctly classified diseased samples. BC's accuracy and TPR is significantly worse compared to RF and SVM, thus reinforcing our inference about the non-linearly separable nature of the samples. RF and SVM, however, have similar performance with accuracies greater than 85% when using our features.

Fig. 3 shows the box plots of accuracy and sensitivity, and ROC curves when we consider *Stage* 2 classification independently. Obviously the values will be higher than those reported in Table 3 (which are based on the original number of samples). The box plots and ROC curves indicate that a high percentage of each sample type is correctly classified by both SVM and RF. This is highly desirable because ultimately we would like to detect the diseased regions from abdominal MRI.

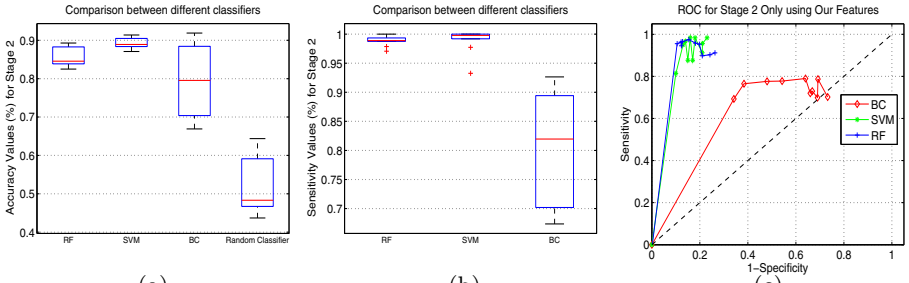

(a) (b) (c)

Fig. 3. Box plots for *Stage* 2 classification: (a) Accuracy; (b) Sensitivity.(c) ROC curves for three methods using RF classifier.

Table 3. Quantitative measures for the second classification stage using different classifiers. Values indicate mean and standard deviation. Sensitivity is the number of correctly classified diseased samples. Specificity is the number of correctly classified normal samples. Accuracy is the total of number of correct classifications (both diseased and normal samples).

	Asy			DTCWT			Our Features		
	SVM	BC	RF	SVM	BC	RF	SVM	BC	RF
Accuracy (%)	81.2 ±1.3	59.1 ±0.9	81.3 ±1.2	81.4 ±1.4	58.4 ±6.1	81.1 ±1.2	87.5 ±2.6	62.8 ±5.4	87.2 ±1.5
Specificity (%)	71.8 ±3.1	36.1 ±4.8	73.4 ±2.4	72.8 ±1.4	37.7 ±2.7	72.2 ±1.9	78.2 ±1.7	42.3 ±4.1	77.1 ±1.6
Sensitivity (%)	84.5 ±1.9	60.5 ±1.2	84.9 ±1.8	86.9 ±1.7	61.3 ±8.2	86.1 ±1.9	91.9 ±2.6	64.8 ±10.7	90.4 ±1.2

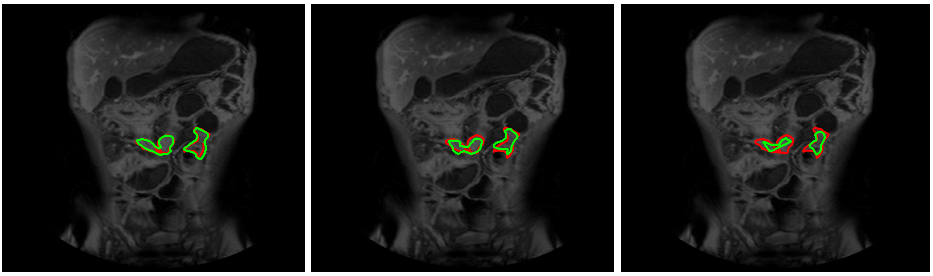

(a) (b) (c)

Fig. 4. Visual results for CD detection in Patient 16 with RF and different features: a) our features, b) *DTCWT* and c) *Asy*. Manually annotated diseased regions are shown in red while the result of automatic detection is shown in green.

Fig. 4 shows visual results for CD detection in Patient 16 using RF and the three features where each voxel is classified as diseased or normal. The manually annotated diseased regions are shown in red while the result of automatic detection is shown in green. The average Dice metric (DM) between manual

annotations and detected regions using our features is 86.5 ± 2.3 (RF), 77.2 ± 3.1 (BC) and 84.9 ± 3.2 (SVM). Our features do a good job in localizing the exact region afflicted with CD without explicit segmentation of the bowel wall.

4 Conclusion

We have proposed a method to identify VOI's in the abdominal MRI that are afflicted with Crohn's disease. Higher order intensity statistics, texture anisotropy and shape asymmetry are used to discriminate between diseased, normal and background regions. Higher order statistics capture image properties that are not discernible to the human eye. Our novel shape asymmetry measure is simple to compute than current approaches, and is informative in detecting diseased regions. Experimental results show that our designed feature vector performs better than Asy and $DTCWT$. Our results indicate that Crohn's disease can be detected from MR images, and thus reduce reliance on invasive procedures like colonoscopy and biopsy. With further improvements of our method in the future, we can hope to build a reliable detection and CD classification system.

Acknowledgements. This research was partly funded from the European Community's Seventh Framework Programme (FP7/2007-2013): the VIGOR++ Project (grant agreement nr. 270379).

References

1. Avni, U., Greenspan, H., Goldberger, J.: X-ray Categorization and Spatial Localization of Chest Pathologies. In: Fichtinger, G., Martel, A., Peters, T. (eds.) MICCAI 2011, Part III. LNCS, vol. 6893, pp. 199–206. Springer, Heidelberg (2011)
2. Bauer, S., Nolte, L.-P., Reyes, M.: Fully Automatic Segmentation of Brain Tumor Images Using Support Vector Machine Classification in Combination with Hierarchical Conditional Random Field Regularization. In: Fichtinger, G., Martel, A., Peters, T. (eds.) MICCAI 2011, Part III. LNCS, vol. 6893, pp. 354–361. Springer, Heidelberg (2011)
3. Berks, M., Chen, Z., Astley, S., Taylor, C.: Detecting and Classifying Linear Structures in Mammograms Using Random Forests. In: Székely, G., Hahn, H.K. (eds.) IPMI 2011. LNCS, vol. 6801, pp. 510–524. Springer, Heidelberg (2011)
4. Bhushan, M., Schnabel, J.A., Risser, L., Heinrich, M.P., Brady, J.M., Jenkinson, M.: Motion Correction and Parameter Estimation in dceMRI Sequences: Application to Colorectal Cancer. In: Fichtinger, G., Martel, A., Peters, T. (eds.) MICCAI 2011, Part I. LNCS, vol. 6891, pp. 476–483. Springer, Heidelberg (2011)
5. Breiman, L.: Random forests. Machine Learning 45(1), 5–32 (2001)
6. Chang, C.-C., Lin, C.-J.: LIBSVM: A library for support vector machines. ACM Transactions on Intelligent Systems and Technology 2, 27:1–27:27 (2011), `http://www.csie.ntu.edu.tw/~cjlin/libsvm`
7. Cheng, J., Tao, D., Liu, J., Wong, D.W.K., Lee, B.H., Baskaran, M., Wong, T.Y., Aung, T.: Focal Biologically Inspired Feature for Glaucoma Type Classification. In: Fichtinger, G., Martel, A., Peters, T. (eds.) MICCAI 2011, Part III. LNCS, vol. 6893, pp. 91–98. Springer, Heidelberg (2011)

8. Fuchs, T.J., Buhmann, J.M.: Computational pathology: Challenges and promises for tissue analysis. Comp. Med. Imag. Graphics 35(7-8), 515–530 (2011)
9. Julesz, B., Gilbert, E.N., Shepp, L.A., Frisch, H.L.: Inability of humans to discriminate between visual textures that agree in second-order statistics – revisited. Perception 2(4), 391–405 (1973)
10. Kelm, B.M., Mittal, S., Zheng, Y., Tsymbal, A., Bernhardt, D., Vega-Higuera, F., Zhou, S.K., Meer, P., Comaniciu, D.: Detection, Grading and Classification of Coronary Stenoses in Computed Tomography Angiography. In: Fichtinger, G., Martel, A., Peters, T. (eds.) MICCAI 2011, Part III. LNCS, vol. 6893, pp. 25–32. Springer, Heidelberg (2011)
11. Kovalev, V.A., Petrou, M., Bondar, Y.S.: Texture anisotropy in 3D images. IEEE Trans. Imag. Proc. 8(3), 346–360 (1999)
12. Liu, Z., Smith, L., Sun, J., Smith, M., Warr, R.: Biological Indexes Based Reflectional Asymmetry for Classifying Cutaneous Lesions. In: Fichtinger, G., Martel, A., Peters, T. (eds.) MICCAI 2011, Part III. LNCS, vol. 6893, pp. 124–132. Springer, Heidelberg (2011)
13. Mary, J.Y., Modigliani, R.: Development and validation of an endoscopic index of the severity for crohn's disease: a prospective multicentre study. Gut. 30(7), 983–989 (1989)
14. Montillo, A., Shotton, J., Winn, J., Iglesias, J.E., Metaxas, D., Criminisi, A.: Entangled decision forests and their application for semantic segmentation of ct images. In: MICCAI, pp. 184–196 (2011)
15. Pauly, O., Glocker, B., Criminisi, A., Mateus, D., Möller, A.M., Nekolla, S., Navab, N.: Fast Multiple Organ Detection and Localization in Whole-Body MR Dixon Sequences. In: Fichtinger, G., Martel, A., Peters, T. (eds.) MICCAI 2011, Part III. LNCS, vol. 6893, pp. 239–247. Springer, Heidelberg (2011)
16. Petrou, M., Kovalev, V.A., Reichenbach, J.R.: Three-dimensional nonlinear invisible boundary detection. IEEE Trans. Imag. Proc. 15(10), 3020–3032 (2006)
17. Rimola, J., Rodriguez, S., garcia Bosch, O., et al.: Magnetic resonance for assessment of disease activity and severity in ileocolonic Crohn's disease. Gut. 58, 1113–1120 (2009)
18. Schunk, K.: Small bowel magnetic resonance imaging for inflammatory bowel disease (2002)
19. Verma, R., Zacharaki, E., Ou, Y., Cai, H., Chawla, S., Lee, S., Melhem, E., Wolf, R., Davatzikos, C.: Multiparametric tissue characterization of Brain Neoplasms and their recurrence usng pattern classification of MR images. Acad. Radiol. 15(8), 966–977 (2008)
20. Zhan, Y., Shen, D.: Deformable segmentation of 3-d ultrasound prostate images using statistical texture matching method. IEEE Trans. Med. Imag. 25(3), 256–272 (2006)
21. Zhang, D., Wang, Y., Zhou, L., Yuan, H., Shen, D.: Multimodal classification of Alzheimer's disease and mild cognitive impairment. Neuroimage 55(3), 856–867 (2011)